JOURNAL OF Applied Polymer SCIENCE

Impact of shape (nanofiller vs. nanorod) of TiO_2 nanoparticle on free-standing solid polymeric separator for energy storage/conversion devices

Anil Arya, Nilesh G. Saykar, A. L. Sharma
Department of Physical Sciences, Central University of Punjab, Mansa Road, Bathinda 151001, Punjab, India
Correspondence to: A. L. Sharma (E - mail: alsharma@cup.edu.in)

ABSTRACT: We report the investigation on examining the impact of nanofiller (NF)- versus nanorod (NR)-shaped titanium oxide (TiO_2) nanoparticle on the structural, electrochemical, transport, thermal, and dielectric properties of the solid polymer electrolyte (SPE). Thin SPE films comprising of poly(ethylene oxide), sodium hexafluorophosphate, and dispersed with TiO_2 NF, TiO_2 NR (synthesized by hydrothermal route) has been prepared via solution cast technique. The shape of nanoparticle influences the morphological and structural properties as observed in field emission scanning electron microscope and X-ray diffraction analysis. The highest ionic conductivity was exhibited by the NR dispersed system and is higher than NF dispersed system for all recorded concentration consistently. It is attributed to the formation of the long-range conductive path with NR when compared with NF. In addition, the electrochemical stability window is much higher (~5 V) than the NF-doped system. Furthermore, the dielectric properties of SPE were investigated and fitted in the complete frequency window (1 Hz–1 MHz; T = 40–100 °C @ 10 °C). It is observed that the NR dispersed system shows higher dielectric strength and low relaxation time with respect to NF dispersed system. The results suggest that the NR dispersed SPE possess enhanced properties and is more appropriate for an application in high energy density solid-state Na ion batteries. © 2018 Wiley Periodicals, Inc. J. Appl. Polym. Sci. **2018**, *136*, 47361.

KEYWORDS: ion transport mechanism; polyethylene oxide; relaxation time; solid polymer electrolyte; TiO2 (nanofiller vs. nanorod)

Received 6 August 2018; accepted 26 October 2018
DOI: 10.1002/app.47361

INTRODUCTION

Due to limited traditional energy resources (fossil fuel, coal, etc.) and increasing demand of green energy, a search of alternative sources of energy (wind, solar, hydro, primary/secondary batteries) become mandatory. The researchers from the past decade have devoted an intensive effort to develop advanced and renewable energy resources. In line of aforementioned efficient energy resources, secondary battery (Li^+/Na^+) getting more attention due to their multidimensional nature of applications (like: boost up in the stationary as well as portable electronic appliances, electronic industry, agriculture sector, and in the transportation industry, etc.).[1–6] As electrolyte is the key component of such batteries and it plays important role in the light of high capacity and safety issue. Since an electrolyte is sandwiched between the two electrodes and provide shuttling of ions into it. Therefore, its importance become manifold when compared with the other components. It certainly overcome the traditional batteries as it suppresses the problems associated (leakage, flammable nature, and safety issue with a liquid part in it.[7–9]

In particular, polymer electrolytes are the most attractive candidate as an alternate of the traditional liquid electrolytes and have advantages enhanced safety, flexibility, and various shape geometries.[10–12] Although gel polymer electrolytes improve the safety issue at large extent, but an extra component (organic/inorganic liquid) reduces the efficiency in terms of short circuiting and heating.[13] To overcome these obstacles, the most feasible approach is the development of free-standing solid polymer electrolyte (SPE) which serve both purpose (organic/inorganic separator and electrolyte) and help multiple ways like: larger surface area for better compatibility to electrodes, miniaturization in shape, and lighter in mass, large efficiencies and so forth.[14] The SPEs comprise of a polymer host matrix having an electron rich group in the polymer backbone and a salt of low lattice energy is dissolved in it. Generally, in the case of polymer electrolytes, the ion migration is mainly through the amorphous phase of the polymer. Since most of the polymers are of semicrystalline nature. Therefore, suppression of the crystalline phase by improving the amorphous phase is another strategy to improve the electrochemical properties. The frequency- and temperature-

dependent conductivity strongly evidence that a favorable ion migration in amorphous phase is attained by the two simultaneous phenomena: (1) hopping and (2) segmental motion or dynamics of polymer matrix.[15–22] It infers the need of amorphous phase in such systems.

The addition of nanoparticle is a most interesting approach that effectively improves the ionic conductivity along with desirable stability (thermal/mechanical/voltage) properties. A number of nanoparticles [titanium oxide (TiO_2), $BaTiO_3$, SiO_2, ZrO_2, etc.] have been investigated and all display the noticeable enhancement of the electrical conductivity along with other key properties. The addition of nanofiller (NF) provides favorable interactions between the: (1) polymer chain and NF surface and (2) cation/anion of salt and surface group of NF. The nanoparticle weakens the polymer cation interaction and also helps in the salt dissociation by interacting with an anion.[23–25] The ion migration is linked with the hopping of ions via coordinating sites and segmental motion of polymer chain. In order to understand the ion transport mechanism in the SPEs, the investigation of dielectric properties parameters (like complex permittivity, complex conductivity, modulus formalism, and relaxation time) are foremost essential.[21,26–29]

The literature lacks reports based on the dispersion of nanoparticle of different shapes and investigations of dielectric and electrical properties has not been reported. Therefore, it has planned to combine the properties of a polymer host matrix with the shape of the nanoparticle. The nanorod (NR) dispersion may overcome the issue of agglomeration observed in the case of NF at a high content. One approach may be that NR may provide continuous percolating conducting path even at low content to the cation migration which gets deteriorates in NF at a high content.

In the solid-state batteries, Li-ion batteries are supposed to be mostly used in the commercial sector, but, some drawbacks such as nonabundant metal, forces to search suitable alternative for large-scale applications. The most appropriate alternative is development of sodium ion (Na; ionic radius: 0.98 Å)-based batteries and has potential to substitute the Li-ion batteries due to advantages such as: (1) high abundance, (2) cost-effective, (3) suitable redox potential [E° (Na^+/Na)= −2.71 V; versus the standard hydrogen electrode], (4) nontoxic nature, and (5) low atomic mass.[30–34] In the present investigation, an attempt is made to study the effect of TiO_2 nanoparticle (NF vs. NR) in the SPE comprising of the poly(ethylene oxide) (PEO)–sodium hexafluorophosphate ($NaPF_6$) matrix. Important studies such as field emission scanning electron microscope (FESEM), Fourier transform infrared (FTIR), impedance study, complex dielectric permittivity, alternating current (ac) conductivity, and modulus formalism were performed for getting insights of the effect of nanoparticle shape on the polymer matrix and ion transport mechanism. The advantage of the dielectric investigation is that it separates out the bulk and interfacial contribution in such a system.

EXPERIMENTAL

Materials

PEO ($M_w = 1 \times 10^6$ g mol^{-1}), $NaPF_6$, and TiO_2 were purchased from the Sigma Aldrich. Acetonitrile was used as a solvent and purchased from the Sigma Aldrich. The polymer and the salt were vacuum dried prior to use.

Synthesis of TiO_2 NRs Using the Hydrothermal Method

The TiO_2 NRs were synthesized using the hydrothermal synthesis reported previously.[35] Briefly, 7 mL of deionized water was mixed with 7 mL of concentrated hydrochloric acid (36.5–38%). The resultant mixture was stirred under ambient conditions for 15 min before adding 0.13 mL of titanium isopropoxide (Sigma Aldrich). The whole mixture stirred till the solution is turns to transparent. After stirring, the mixture was placed in a Teflon-lined stainless steel (SS) autoclave of 25 mL volume and heated to 180°C for 24 h. On the completion of the reaction, the resultant precipitate was washed two to three times with distilled water.

Preparation of Polymer Electrolytes

All the polymer electrolytes are prepared by the standard solution cast technique. The salt ratio (O/Na^+) is kept constant (8:1) that is an optimized value for high ionic conductivity and has been calculated considering oxygen as coordinating site of PEO.[36] First, the 0.5 g of PEO is dissolved in the acetonitrile (15 mL) by stirring until a homogenous solution is obtained. After that, an appropriate salt (O/Na^+ = 8:1) is added to the polymer solution and again stirred for 6–8 h. A transparent polymer salt solution is obtained. Now, the appropriate amount of the varied NF and NR is added separately in 5 mL solvent and sonicated for half an hour to disperse nanoparticles properly. After sonication, the nanoparticle solution is added to the polymer salt solution and stirred for 18–20 h. Finally, the obtained solution is cast on the glass Petri dishes and left for drying at room temperature. After that, kept in a vacuum oven to completely remove the residual solvent. Now, the films are peeled off from the Petri dishes and kept in the desiccator (with silica gel inside) for performing the characterizations further.

The samples are designated as 1 NF, 2 NF, 3 NF, 4 NF (TiO_2 NF) and 1 NR, 2 NR, 3 NR, 4 NR (TiO_2 NR). Figure 1(a–c) shows the interaction between the polymer, salt, nanoparticle (NF/NR) and Figure 1(d) shows the schematic diagram of solution cast technique.

Characterization of Materials

Structural and Microstructural Studies. X-ray diffraction (XRD) (Bruker D8 Advance) has been performed for the determination of *d*-spacing, interchain separation and recorded with Cu Kα radiation (λ = 1.54 Å) in the Braggs angle range (2θ) from 10° to 60°. The FTIR spectra (Bruker Tensor 27, Model: NEXUS–870) are recorded in absorbance mode over the wave-number region from 600 to 3500 cm^{-1} to probe the presence of various interactions such as polymer–ion, ion–ion interaction, and complex formation.

Electrical Analysis. The ionic conductivity (σ) has been measured by complex impedance spectroscopy in the frequency range of 1 Hz–1 MHz using the CHI760 electrochemical analyzer (T = 40–100 °C with temperature controller: Marine India). An ac sinusoidal signal of 10 mV has been applied to the cell configuration SS|SPE|SS where SPE films are sandwiched between two

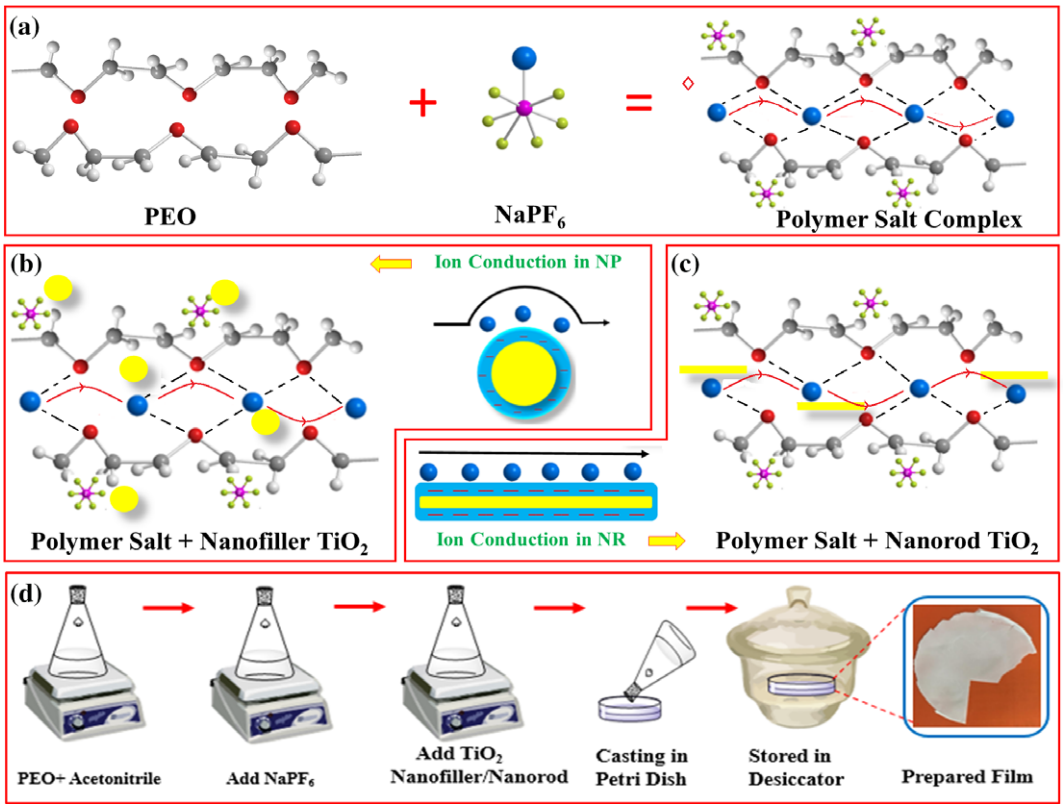

Figure 1. (a) Polymer salt complex formation, (b) role of NF in ion transport, (c) role of NR in ion transport, and (d) schematic flowchart of solution cast technique. [Color figure can be viewed at wileyonlinelibrary.com]

SS electrodes. The intercept between the semicircle at high frequency and tilted spike at low frequency were taken as the bulk resistance (R_b). The electrical conductivity (σ) value was obtained using eq. (1):

$$\sigma_{dc} = \frac{1}{R_b}\frac{t}{A} \quad (1)$$

where "t" is the thickness (cm) of the polymer film (100–115 μm), R_b is the bulk resistance (Ω), and A is the contact area (cm^2) of working electrode. The thermal activation energy for ionic transport has been estimated from the slope of the linear fit of the Arrhenius plot. The linear variation in log (σ/S cm^{-1}) versus 1000/T plot suggests a thermally activated process represented by $\sigma = \sigma_o \exp(-E_a/kT)$, where σ_o is the constant pre-exponential factor and E_a is the activation energy. The parameter T stands for the absolute temperature and k for the Boltzmann constant. The ion transference number was obtained via *i-t* characteristics with a voltage of 10 mV. using *SS|SPE|SS* cell and using the following eq. (2):

$$t_{ion} = \left(\frac{I_t - I_e}{I_t}\right) \times 100 \quad (2)$$

Dielectric Spectroscopy. The impedance data are transformed into the dielectric constant, dielectric loss, complex conductivity data which is further transformed into the real and imaginary parts of the modulus. All plots are fitted with corresponding equations by Origin 8 software to evaluate the various parameters that enable us to explore the ion dynamics.

Stability Analysis. Thermal stability of the synthesized SPE films has been investigated using thermogravimetric analysis (TGA; SHIMADZU DTG-60H) under dynamic temperature conditions from 30 to 600 °C, in a controlled nitrogen atmosphere at a constant heating scan rate of 10 °C min^{-1}. The linear sweep voltammetry (LSV) was performed to obtain the operating voltage of the electrolyte.

RESULTS AND DISCUSSION

Structural and Microstructural Analysis

FESEM Analysis. Figure 2(a) shows the FESEM of the TiO_2 NF and the particles are spherical with an average size of ~25 nm. Figure 2(b) clearly indicates the rod-type morphology as prepared by the hydrothermal method. The diameter of the TiO2 NR is 30–70 nm while the length is about 800–1000 nm.

Figure 3(a) shows the FESEM micrograph of the pure PEO and it shows the rough surface with cracks that evidence the semicrystalline nature of the PEO. On the addition of the salt, crystalline nature disrupts and change in morphology is evidenced as shown in Figure 3(b). The Lewis-acid–base interactions evidence the alteration in the morphology and enhancement of the amorphous content is observed. Figure 3(c) shows the energy-dispersive X-ray (EDX) spectra of the polymer salt matrix dispersed with the 3 NF and it evidences the dispersion of the NF in the polymer matrix. Figure 3(d) depicts the polymer salt matrix with dispersed NR inside (3 NR). It is clearly visible that the rod type structures are inside the polymer matrix and polymer salt matrix

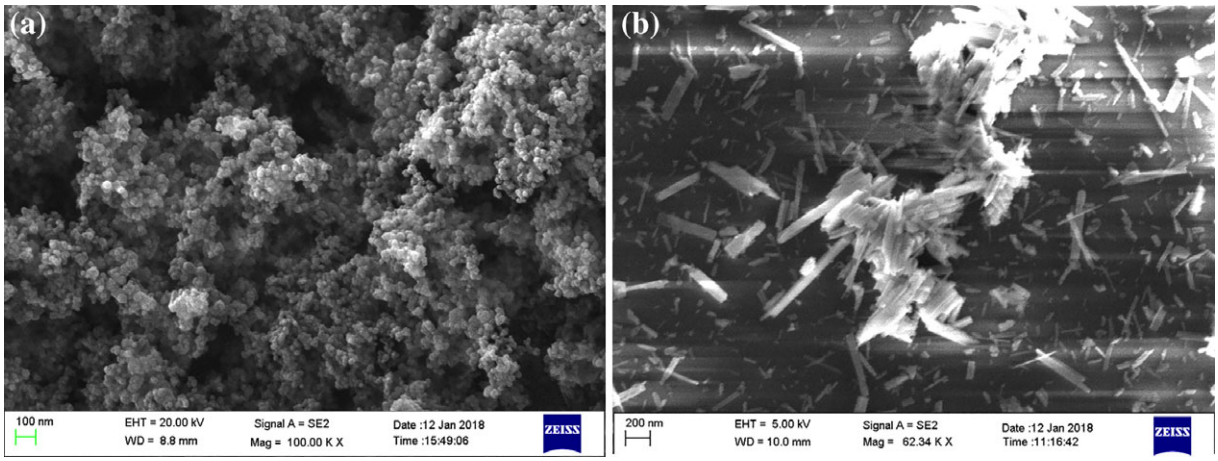

Figure 2. FESEM micrographs of (a) commercial TiO_2 NF and (b) TiO_2 NR prepared by hydrothermal method. [Color figure can be viewed at wileyonlinelibrary.com]

is enveloped on the NR (shown by circles). Although the length of the NR is not identical, the micrograph confirms the nanocomposite formation.

Figure 3(e) depicts the EDX spectra of the 3 NR system and evidences the formation of the polymer nanocomposites (PNCs). Another important approach is the elemental mapping that

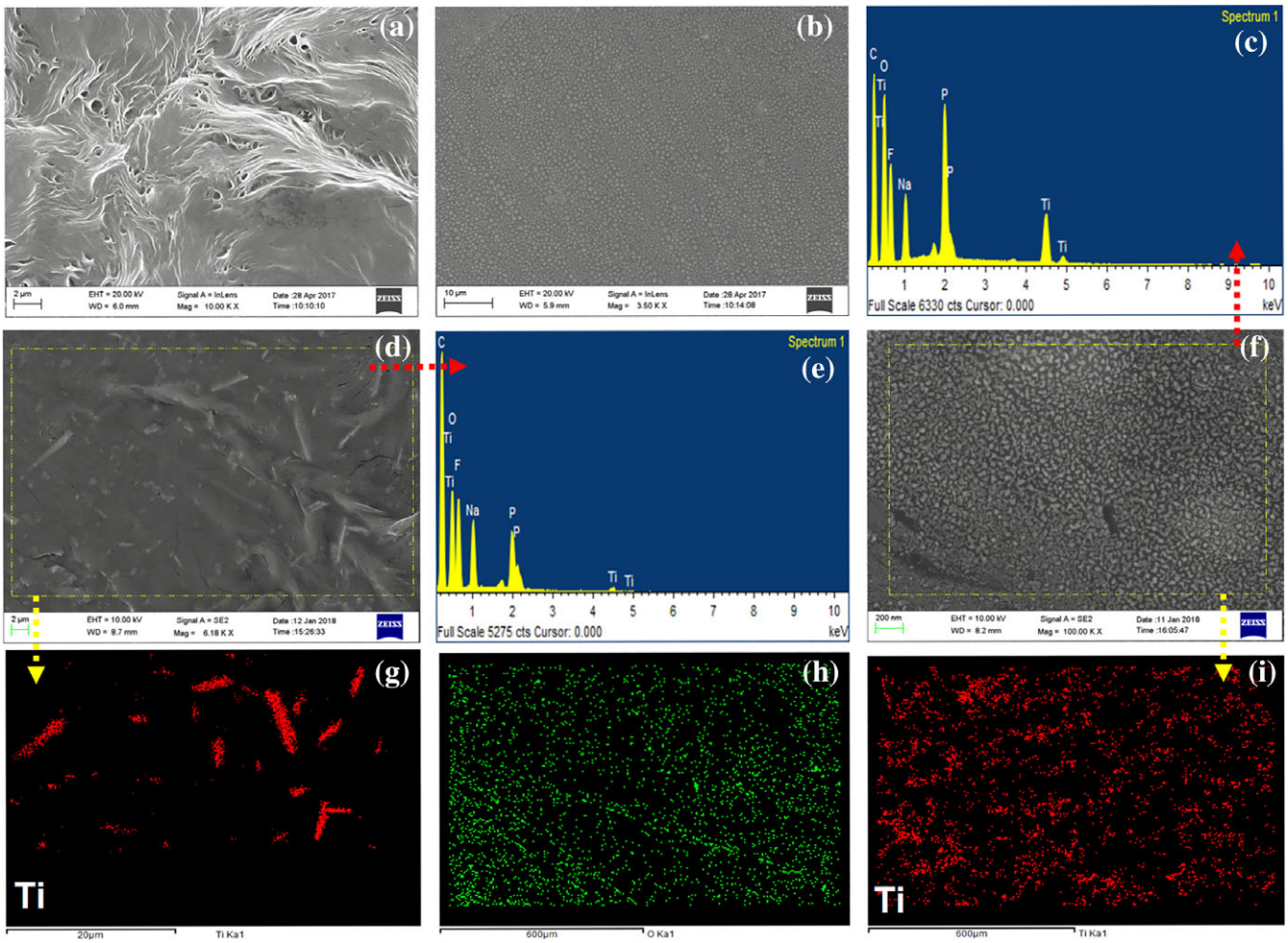

Figure 3. FESEM micrographs of the (a) pure PEO, (b) polymer salt complex, (c) EDX of optimum sample with TiO_2 NF, (d) PEO–$NaPF_6$–3NR, (e) EDX of 3NR system, (f) PEO–$NaPF_6$–3 NF, (g) elemental mapping of Ti in polymer electrolyte with 3NR, (h) elemental mapping of O in 3 NF, and (i) elemental mapping of Ti in 3 NF system. [Color figure can be viewed at wileyonlinelibrary.com]

confirms the nanoparticle (NF/NR) dispersion. Figure 3(f) shows the micrograph of the polymer salt matrix with TiO_2 3 NF. It may be noticed that the NF is uniformly dispersed in the polymer matrix attributed to the polymer–ion–NF interaction. Figure 3(g, i) shows the elemental mapping of element Ti for the NR and NF, respectively. It suggests the clear indication of the rod-like morphology and NF uniform dispersion. Furthermore, the effect of the nanoparticle shape will be explored in the impedance study section.

XRD Analysis. The XRD has been performed to qualitatively identify the SPE structural properties by analyzing the peak intensity and broadening. Figure 4 depicts the X-ray diffractogram of the PEO as a host polymer, polymer salt and polymer salt dispersed with NF and NR in the angular range 2θ from 10° to 40°. The XRD pattern of the pure PEO shows the two sharp crystalline peaks at 2θ = 19.3° and 23.2°, associated with (120) and (112), (032) planes, respectively.[37]

The salt added is $NaPF_6$ and exhibits sharp and intense diffraction peaks at 20°, 22°, 32°, and 44°. When salt is added in the PEO, then the peak of pure PEO remains there but now with a reduction in intensity is observed for peak located @ 19.3° and broadening for peak located @ 23.2°.

The absence of any peak associated with salt indicates the complete salt dissociation. The two additional peaks near 13° and 16° are not of PEO and salt which may be attributed to the formation of a long-range order owing to the presence of ion multiplets (as Na_2X^+, NaX_2^-, etc.).[38,39] After the addition of nanoparticle (1 NF–4 NF), the small change in intensity is observed for the (120) peak while major change is observed for the peak (112)/(032). This indicates the modification of the polymer chain arrangement and evidences the increase of the amorphous content owing to the interaction polymer–TiO_2 NF. After the incorporation of NR in the polymer salt matrix, (120) and (112)/(032) peak are highly suppressed, indicating the reduction of the crystallinity. This suggests the NR interaction with polymer salt matrix. Also, the characteristics peak of the salt was not present in the NF and NR dispersed system which confirms the complete dissociation of salt. This confirms the reduction of the crystallinity due to the lowering of chain reorganization tendency. The *d*-spacing between the diffraction planes was obtained using Bragg's formula $2d\sin\theta = n\lambda$ and interchain separation (R) using the equation $R = 5\lambda/8\sin\theta$.[40] The recorded parameters are summarized in Table I.

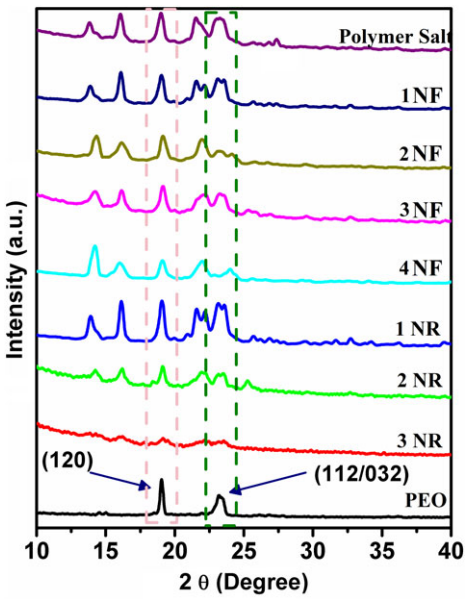

Figure 4. XRD diffractograms of SPE. [Color figure can be viewed at wileyonlinelibrary.com]

FTIR Spectroscopy. FTIR spectroscopy is the powerful technique to get information about the interactions in the polymer matrix and the functional groups. Figure 5 shows the FTIR spectra of the PNCs with different contents of the NF and NR in the wavenumber region 600–3000 cm^{-1}. Figure 5(a) shows the fingerprint region of FTIR spectra of the pure PEO and the fundamental peak of the PEO are observed. The peak located near 950, 1100, 1230, 1280, and 1340 cm^{-1} are assigned to the C–O stretching vibration mode, symmetric and asymmetric C-O-C stretching mode, CH_2 asymmetric/symmetric twisting mode, and CH_2 bending mode, respectively. The peak at 1100 cm^{-1} is attributed to the amorphous content of the PEO.[41] The symmetric and asymmetric vibrations of C-H stretching mode of CH_2 group in PEO are observed near 2900 cm^{-1}. Now, on the addition of the salt, there is a change in the peak intensity, peak position, and the peak shape. On the addition of salt, the fundamental peak of PEO gets broadened and a shoulder appears. This alteration is attributed to the cation coordination with the ether group of the polymer host. The shift in peak position on the addition of salt in the region 800–1000 cm^{-1} is attributed to the alteration in the polymer backbone. When salt gets separated in the cations and anions then cation gets coordinated with ether group while anion is supposed to attach with the methyl group (CH_2) of the polymer backbone. The peak broadening in the peak located at 950 cm^{-1} after the dispersion of NR is effective than NF and it indicates that crystallinity is reduced effectively by NR as compared to NF.[42] Furthermore, the effect of the addition of salt is also visible in the peak located at 2900 cm^{-1}.

On the addition of the salt, peak shifts toward higher wavenumber side and is split in two. Both the above key points evidence the complex formation.[43] In the PNC, the fundamental group of the PEO, $NaPF_6$, and nanoparticles is observed; it indicates the complex formation. Addition of the NF and NR alters the peak located at 1100 cm^{-1} associated with C-O-C stretching and peak get broadened and splits in two after NF and NR dispersion.

The peak splitting and shifting toward the lower wave-number side confirms the dominance of the Na^+–O interaction owing to the better salt dissociation. The peak broadening suggests the enhancement in the amorphous content. From the FTIR analysis, it may be concluded that the salt gets dissociated properly in the polymer matrix and dispersion of the NF and NR alters the polymer chain arrangement that will support the fast ion migration which will be analyzed in the upcoming section.

Table I. Values of 2θ (°), *d*-Spacing (Å), and *R* (Å) of SPE Dispersed with NF and NR

	(120) Reflection peak parameters			(112)/(032) Reflection peak parameters		
Sample	2θ (°)	*d*-spacing (Å)	*R* (Å)	2θ (°)	*d*-spacing (Å)	*R* (Å)
PEO	19.07	4.65	5.81	23.28	3.81	4.76
Polymer salt	19.00	4.66	5.82	23.18	3.83	4.78
1NF	19.00	4.66	5.82	23.10	3.84	4.80
2NF	19.15	4.63	5.78	23.26	3.81	4.77
3NF	19.15	4.63	5.78	23.26	3.81	4.77
4NF	19.12	4.63	5.79	23.92	3.71	4.65
1NR	19.05	4.65	5.81	23.13	3.84	4.80
2NR	19.09	4.64	5.80	23.15	3.83	4.79
3NR	19.17	4.62	5.78	23.18	3.83	4.78

Electrical Analysis

Impedance Spectroscopy and Conductivity Analysis. The electrical conductivity of the prepared PNC films has been evaluated using the impedance spectroscopy by sandwiching PNC between two SS ion blocking electrodes with a voltage signal of ~20 mV in the temperature range 40–100 °C. The Nyquist plot is displayed in Figure 6(a) (in log–log representation) for the 3NR system. The log–log presentation has various advantages over the traditional Nyquist plot as elaborated by Jonscher.[44,45] The dip in the plot on the *x* axis is associated with the bulk resistance in the polymer electrolyte system. With the increase of the temperature, the dip shifts toward the lower value as shown by the arrow. The lowering of the bulk resistance indicates the thermal activation of the charge carriers which results in an enhancement of the conductivity. It may be observed from the plot that right side of the graph (in low frequency) is associated with double-layer capacitance effect owing to the ion blockage at the end of blocking SS electrodes.[46] With the increase in temperature, this effect increases due to the availability of more free ions for double-layer formation. The ionic conductivity depends on: (1) concentration of the mobile ions, (2) ion charge, and (3) ion mobility (how easily an ion is moved through the solid) and expressed as; $\sigma = ne\mu$.[47] The ionic conductivity of all SPEs was calculated by using eq. (1).

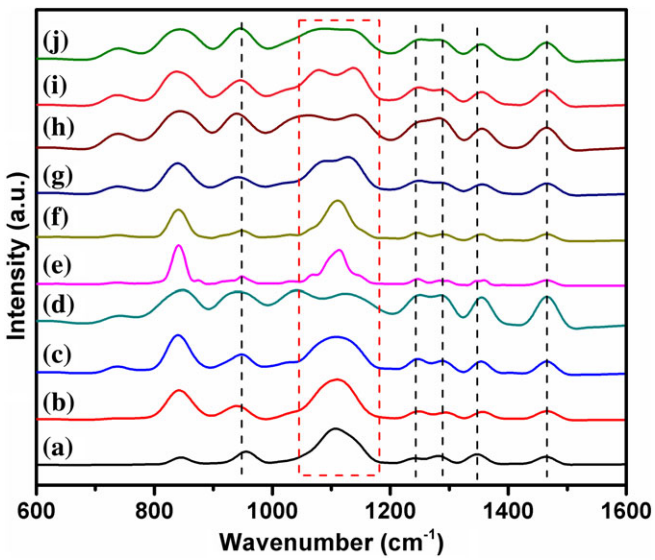

Figure 5. FTIR spectra of the SPE (a) PEO, (b) PEO-$NaPF_6$, (c–f) 1NF-4NF, and (g–j) 1NR-4NR. [Color figure can be viewed at wileyonlinelibrary.com]

On comparing the ionic conductivity values of NF and NR dispersed system from Figure 6(b), it may be noticed that the highest ionic conductivity is for the PNC dispersed with NR as compared to the NF. The observed increase in the conductivity may be due to the increased surface area of interaction for NR and it provides a continuous conducting path which promotes long-range ion migration [Figure 6(d)]. Therefore, the nanoparticle creates a continuous path for a long time leading to enhanced ionic conductivity. In brief, the enhancement in the conductivity may be due to the following reasons: (1) formation of continuous conducting pathways, (2) lowering of the crystallinity, and (3) better salt dissociation.[48] However, at high NF/NR content, decrease in the ionic conductivity is observed that may be due to the agglomeration of NF/NR which results in the formation of ion pairs or may block the path for ion migration by restricting the polymer chain motion. The maximum ionic conductivity was obtained for the NR dispersed polymer electrolyte as compared to NF in the temperature range 40–100 °C.

Temperature Dependence of Ionic Conductivity. The ionic conductivity of the prepared PNC film has been further investigated in the temperature range of 40–100°C. Figure 6(b) displays the variation of conductivity with temperature for different polymer electrolytes dispersed with NF and NR. It is observed that with an increase in temperature, conductivity increases for all samples and may be due to the enhanced polymer chain flexibility which results in high ion mobility and hence the ionic conductivity. The increase of temperature increases the free volume available for the ion migration due to the expansion of polymer chains and provides easy accesses to cation dynamics with the coordinating sites provide by the polymer chains.[16] The increase in the segmental motion of the polymer chains results in faster ion migration and ionic conductivity of the composite polymer electrolyte increases. It was found that TiO_2 NRs were able to provide effective percolation conductive path in the polymer salt matrix.

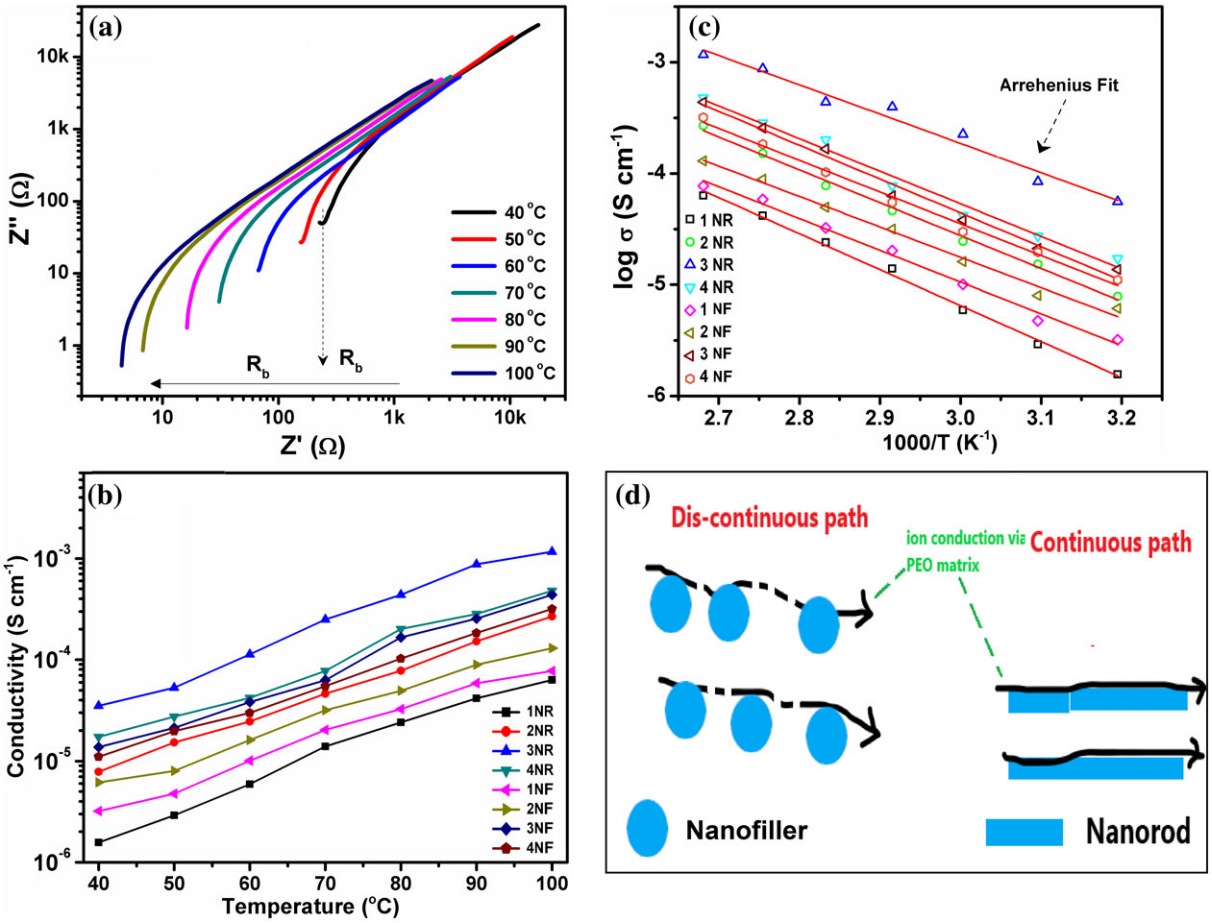

Figure 6. (a) Nyquist plot for the 3NR sample at a different temperature, (b) variation of conductivity for prepared PNC with temperature, (c) Arrhenius plot of the temperature-dependent conductivity of the PNC with NF/NR, and (d) ion conduction pathways for NF and NR. [Color figure can be viewed at wileyonlinelibrary.com]

Thermal Activation Energy Measurement. Figure 6(c) shows the linear variation in log (σ/S cm^{-1}) versus 1000/T plot and the red solid line is the Arrhenius fit. The activation energy of the PNC was obtained by the Arrhenius equation, $\sigma = \sigma_o \exp\left(-\frac{E_a}{kT}\right)$, where σ_o is the constant pre-exponential factor and E_a is the activation energy. The parameter T stands for the absolute temperature and k for the Boltzmann constant. The activation energy is the energy required to jump an ion from one coordinating site to another and probably enable us to find the favorable environment for the ion migration.[49,50] Figure 6(c) shows the Arrhenius fit and for all samples, it shows good agreement with the experimental data. The activation energy was lowest for the 3NR sample that confirms the highest ionic conductivity associated with it (Figure 7). This reduction of the activation energy value is attributed to the increased free volume and faster chain segmental motion.

Transference Number Measurement. To support the ionic conductivity study, measurement of the ion transference number (t_{ion}) is crucial of the prepared system. The polarization plot as a function of time (@ RT) for the NF and NR dispersed system is shown in Figure 8. It may be noticed from the plot that initially current is very high ($I_t = I_e + I_{ion}$) and is a contribution from the flow of both ions and electrons, with an increase of time decreases reached to the steady state after some time. The initial decrease in the current is due to the polarization mechanism that

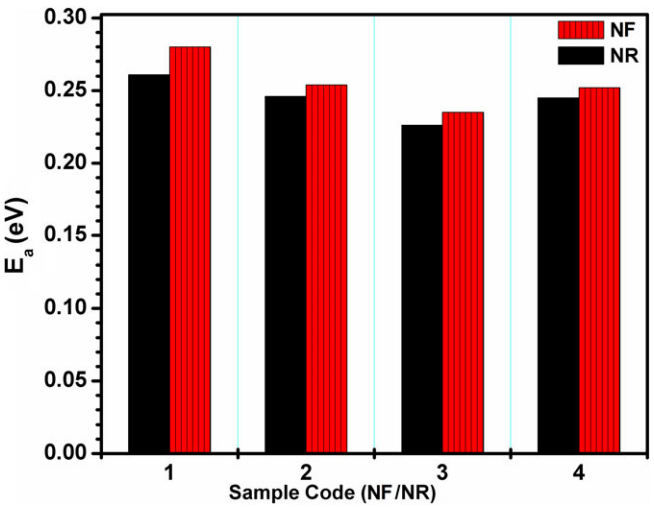

Figure 7. Comparison of activation energy for nanoparticle and NR dispersed systems. [Color figure can be viewed at wileyonlinelibrary.com]

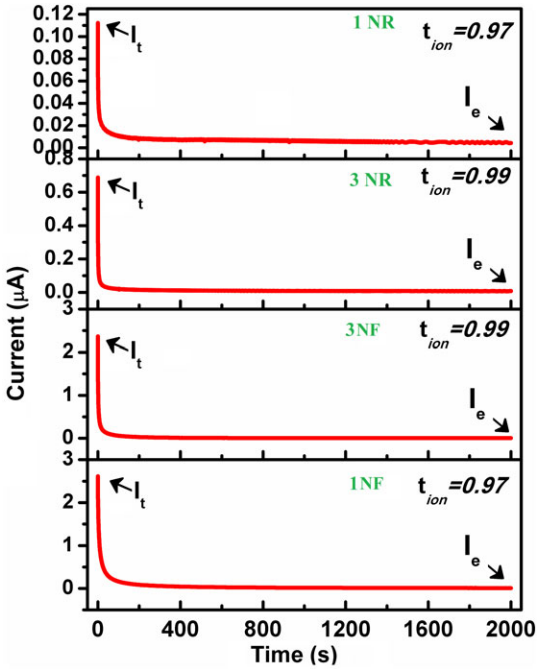

Figure 8. Polarization curve to determine ion transference number of SPEs. [Color figure can be viewed at wileyonlinelibrary.com]

leads to ion accumulation at electrodes and the residual current is due to electron only as ion get blocked with time. The ion transference number was 0.97–0.99 for all systems that evidences the predominantly ionic nature of the prepared system with a negligible electronic contribution (t_e = 0.01–0.03) and is obtained using eq. (2). The high value of the ion transference number is due to the faster cation migration in the polymer matrix dispersed with nanoparticles, which is explained as follows.

The cation of the salt interacts with the electron rich group (ether group) of the polymer host and hence alters the polymer chain arrangement that reflects the enhancement of the amorphous content. This enhancement in the amorphous content facilities the faster ion migration that leads to enhanced ion transference number. The high value of the ion transference number (0.99) is sufficient for application in the solid-state batteries.[51]

Dielectric Studies

Complex Permittivity Analysis. The complex dielectric permittivity (ε^*) comprise of the real (ε') and imaginary part (ε'') that may combined by equation expressed as:

$$\varepsilon^* = \varepsilon' - j\varepsilon'' \tag{3}$$

The dielectric constant (ε') and dielectric loss (ε'') are two very important properties that may be taken care seriously for their suitability of polymer electrolyte in energy storage/conversion devices. The dielectric constant (ε') depicts the polarizing ability (during formation of hetero charge layer) on application of the electric field which creates ion accumulation on electrodes/electrolyte interface. The dielectric loss (ε'') indicates the loss in the polymer matrix due to ion oscillation and dipoles alignment on the application of field.[52–54] Figure 9(a–f) displays the plot of real and imaginary parts of complex permittivity for NF and NR dispersed PNCs. The frequency-dependent real and imaginary part of the complex permittivity has been analyzed further by eqs. (4a) and (4b)

$$\varepsilon' = \epsilon_\infty + \frac{\Delta\varepsilon\left(1 + x^\alpha \cos\frac{\alpha\pi}{2}\right)}{1 + 2x^\alpha \cos\frac{\alpha\pi}{2} + x^{2\alpha}} \tag{4a}$$

$$\varepsilon'' = \Delta\varepsilon \frac{x^\alpha \sin\frac{\alpha\pi}{2}}{1 + 2x^\alpha \cos\frac{\alpha\pi}{2} + x^{2\alpha}} \tag{4b}$$

Here, ε_s is the static dielectric constant ($x \to 0$), ε_∞ is the dielectric constant ($x \to \infty$), $x = \omega\tau$; ω is the angular frequency of applied field, and τ is the Debye relaxation time (reciprocal of jump frequency in the absence of external electric field). Here, α is the distribution (power law) exponent of the material sample.[55,56] The plot indicates the low frequency dispersion followed by the high frequency saturation. The solid red line is the best fit to the experimental data point by eqs. (4a) and (4b). Figure 9(a–f) shows the perfect agreement between the experimental and simulated data almost in the entire frequency window for both real and imaginary parts of the complex permittivity (@ 40 °C). It may be noted that in high frequency, there is a slight deviation from the experimental data. The above deviation may be attributed to the dominance of dielectric relaxation of polymer chain (with cation) in high-frequency window. Same has been reported in the earlier report also and may be resolved by simulating the experimental data with Havriliak and Negami equation.[57,58]

Furthermore, to investigate the effect of temperature on the complex permittivity, the temperature variation of the optimized sample (3NR) has been performed in the temperature range (40–100 °C). It may be obtained from Figure 9(e,f) that with an increase of temperature, both simulated and experimental data point's show good agreement as compared to lower temperature and may be due to the shift of the dielectric relaxation region toward the high frequency. All system demonstrates the high value of the dielectric constant at a lower frequency and decrease with the increase of frequency. As the prepared electrolytes are ionic conductors, so the presence of electrode polarization (EP) is a fundamental property of ionic conductors.[46,59–61]

The low value may be due to the dominance of the dielectric polarization contribution from salt dissociation (with NF and NR dispersion) and electron rich group of the polymer. The former one creates ion accumulation region on blocking electrodes (SS) owing to the availability of more free number of charge carriers, while later one is due to the conformational change in the polymer chain on the application of field. The hindrance to the long-range ion migration may be another key point responsible for ion accumulation. Now, when frequency increases, then the dielectric constant decreases due to dielectric relaxation mechanism. The rapid change of electric filed restricts the rotation/translational motion and ion diffusion is blocked due to the inability of dipoles to rotate themselves in the direction of the electric field.[62,63]

Figure 9(c,d) shows the frequency-dependent dielectric loss (ε'') and decreases with the increase of the frequency. There is no peak for the EP in the dielectric loss spectra. The solid red line

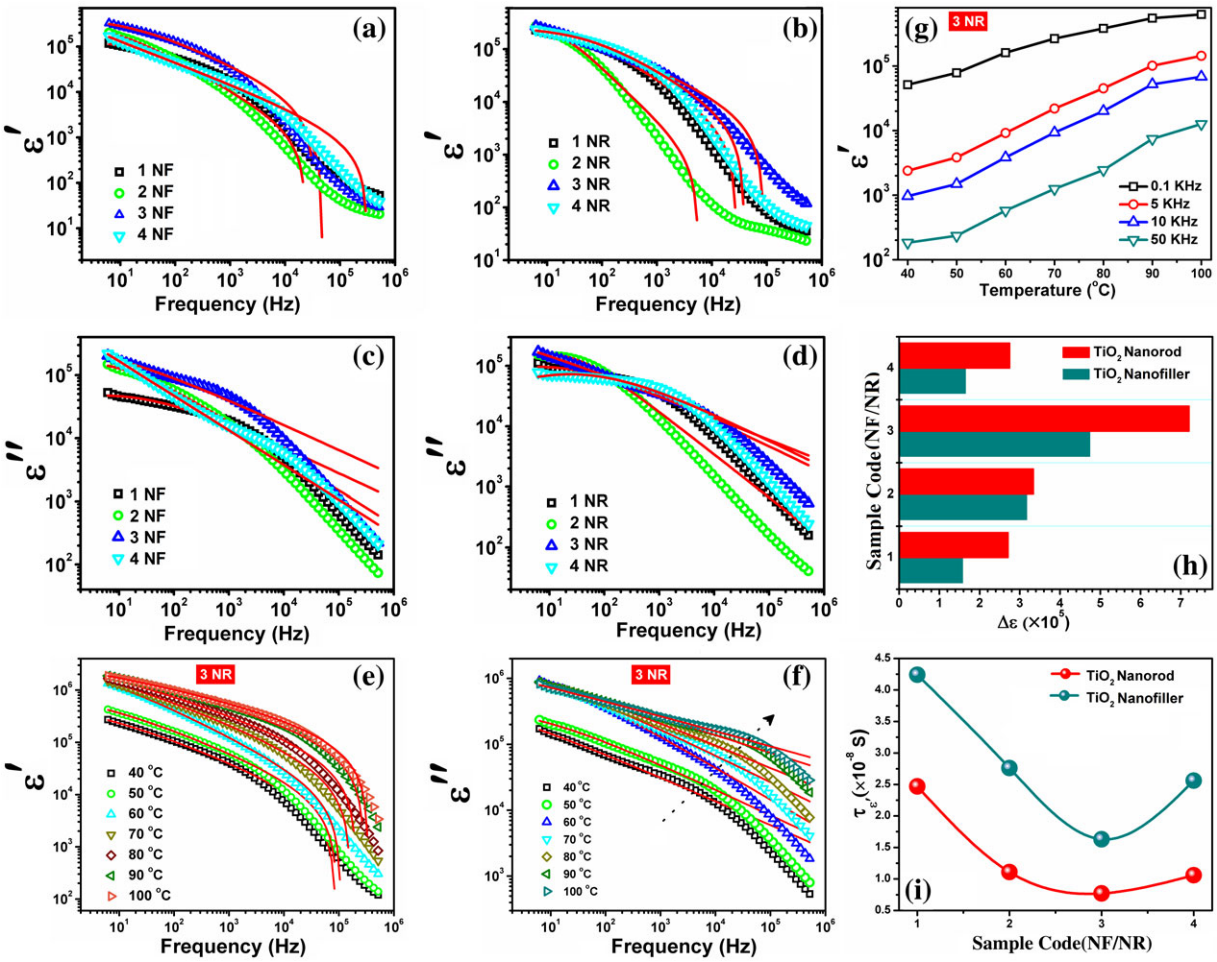

Figure 9. Variation of real part of complex permittivity (a) for nanoparticle, (b) NR, and imaginary part of dielectric permittivity, (c) nanoparticle, and (d) NR (@ 40°C). Temperature-dependent (e) real part and (f) imaginary part of complex permittivity for 3NR sample. The solid red line is the fitted plot. (g) The variation of dielectric constant with temperature for 3NR sample, (h) variation of dielectric strength, and (i) relaxation time for various nanoparticles and NR-based PNCs. [Color figure can be viewed at wileyonlinelibrary.com]

depicts the fitted plot. The dielectric loss originates from the generation of internal heat due to periodic reversal of field. The low-frequency dielectric loss is attributed to the direct current (dc) resistivity while the high-frequency loss is due to dipole rotation from low to high energy states.[64] Figure 9(f) shows the temperature-dependent dielectric loss against the frequency for the 3NR sample. In the high frequency, dielectric relaxation is observed owing to the segmental motion of cation coordinated polymer chains. The dielectric relaxation is observed to shift toward the high frequency with an increase of temperature (indicated by dotted arrow). This indicates the faster segmental relaxation of polymer chains due to increased polymer flexibility which increases the ionic conductivity and ion mobility.[65–67]

It is also observed in Figure 9(e,f) that both dielectric constant and dielectric loss increase with the increase of the temperature and may be due to the increase in a number of charge carriers (n α T) owing to the better salt dissociation.[68] Figure 9(g) displays the variation of dielectric constant with temperature at different frequencies for the 3NR sample. It is observed that dielectric constant is higher for lower frequency and decreases with an increase of frequency. Furthermore, with an increase of temperature, dielectric constant increases at all frequencies. This increase is attributed to the better salt dissociation and hence the availability of a more free number of charge carriers.[69,70] In the case of polymer electrolytes, the number of charge carriers (n) is related with dissociation energy and the dielectric constant.[71] The equation is expressed as eq. (5).

$$n = n_o \exp\left(-\frac{U}{\varepsilon' kT}\right) \tag{5}$$

As the real part of complex permittivity, that is, dielectric constant indicates the storage capacity of ions in the material. As dielectric constant increases with temperature, it results in more salt dissociation in the cations and anions and hence the increase in a number of charge carriers participating in the conduction process. At higher NF/NR content, dielectric constant decreases which may be due to the formation of NF/NR aggregation that blocks the ion conducting pathways and consequence is the reduction of ionic conductivity.[63] The above equation indicates the increase in the number of charge carriers. As dielectric constant depicts the storage capacity of ions and high value of dielectric constant imitates the additional number of ions stored. The increase of dielectric polarization

is also enhanced by the increased segmental motion of polymer chain due to increased polymer flexibility and segmental motion of polymer chain.[72,73]

Figure 9(h) shows the variation of dielectric strength ($\Delta\varepsilon = \varepsilon_s - \varepsilon_\infty$) for NF and NR dispersed polymer electrolyte. It is observed that with an increase of NF and NR content dielectric strength increases with a maximum for 3NF and 3NR sample. Further increase of content decreases the dielectric strength which may be due to the nonuniform dispersion of nanoparticle and NR in the polymer matrix. However, the dielectric strength is higher for the polymer nanocomposites dispersed with NR as compared to the NF in all combinations. The increase of dielectric strength may be due to the higher surface area associated with NR as compared to NF. The frequency- and temperature-dependent dielectric properties suggest the key role of nanoparticle shape on the ion dynamics. Figure 9(i) shows the variation of relaxation time ($\tau_{\varepsilon'}$) for PNCs dispersed with nanoparticle and NR. It is clearly observed that the relaxation time decreases with the increase of the nanoparticle and NR content with minima for the 3NF/3NR sample. Comparatively, the relaxation time was lower for the PNCs dispersed with NR and is in good agreement with the impedance results which shows the highest ionic conductivity for this system (3NR). The above analysis confirmed that the rod-shaped morphology plays an effective role in enhancing the ion migration as evidenced by the decrease of the relaxation time and increase of dielectric strength. The decrease of the relaxation time indicates the increase in the flexibility as well the amorphous content in PNC matrix and hence confirm the faster/easier segmental motion of polymer chains.[74,75] The increase in dielectric strength [Figure 9(h)] is in strong correlation with the decrease of relaxation time and the ionic conductivity. The ionic conductivity increases with the increase of the number of the free charge carriers which is directly linked with the dielectric strength. The 3NR sample exhibits the highest ionic conductivity and dielectric strength which suggest the faster ion conduction for this sample and hence the low relaxation time as evidenced in Figure 9(i).

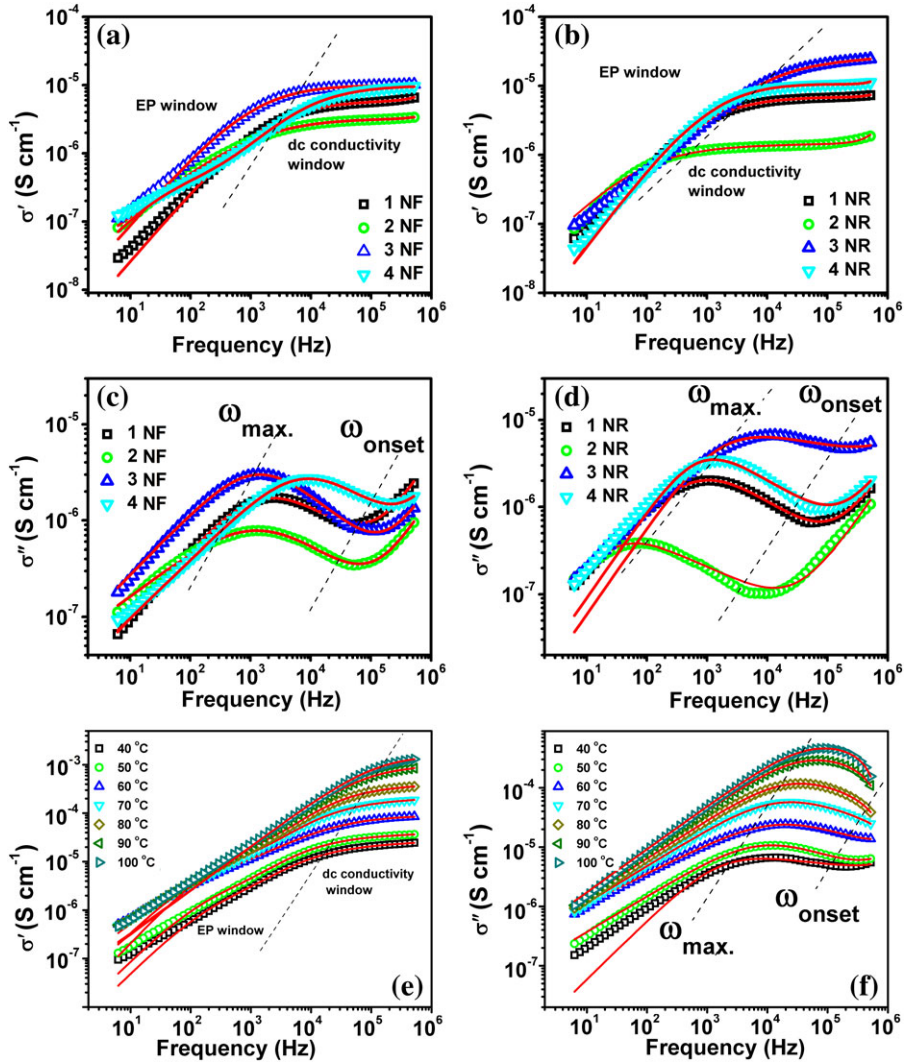

Figure 10. Variation of real part of complex conductivity (a) for nanoparticle, (b) NR, and imaginary part of complex conductivity, (c) nanoparticle, and (d) NR (@ 40°C). Temperature-dependent (e) real part and (f) imaginary part of complex permittivity for 3NR sample. The solid red line is the fitted plot. [Color figure can be viewed at wileyonlinelibrary.com]

Complex Conductivity Analysis. Figure 10(a–d) shows the frequency-dependent real (σ') and imaginary (σ'') part of the electrical conductivity for SPE dispersed with NF/NR. The variation of σ' and σ'' explores the three phenomena: (1) EP region (*low-frequency window*), (2) dc conductivity region (*intermediate frequency window*), and (3) conductivity dispersion region (*high-frequency window*).[76] In the low-frequency window, the σ' plot shows the huge decrease in σ',attributed to the dominance of EP effect at electrode–electrolyte interface owing to the charge accumulation. It indicates the formation of the electric double layers at the electrode–electrolyte interface.[67,77,78] With increase of the frequency, in the intermediate frequency region almost frequency-independent plateau in σ' is observed and is associated with the macroscopic dc conductivity (σ_{dc}). The higher value of dc conductivity suggests the high crossover frequency or lowering of relaxation time.[79–81] In this region, the hopping of the charge carriers from one coordinating site to another via the polymer matrix results in long-range ion diffusion.[82] Further increase of frequency leads to the change in the slope of the conductivity versus frequency plot and is attributed to the dispersive region [-Figure 10(a,b)]. Also for the polymer electrolyte dispersed with NR the dc conductivity is higher and it suggests that the crossover frequency shift toward higher frequency, hence faster ion migration. The obtained frequency dispersion may be explained using the jump relaxation model and is typical behavior of ionic conductors.[56,83–85] It proposes that in the low-frequency window, that is, $\omega \rightarrow 0$, an ion can jump from one coordinating site to another successfully and contributed to the dc conductivity. Now, when the frequency is above the crossover frequency, then the lowering of relaxation time evidences the increase in the ion hopping probability back to initial site with null probability of forward ion hopping to new site. In the high frequency, the possibility of correlated forward–backward hopping along with the relaxation of the dynamic cage potential leads to the dispersion observed in the high frequency according to universal Jonscher power law. Further it may be noticed from the plot [Figure 10(a–d)] that the frequency-independent plateau shifts toward the high frequency with NF/NR dispersion and suggests the increased amorphous content as well as faster segmental motion of the polymer chains. It was evidenced from Figure 9 (i) that relaxation time reduction is more for NR dispersed system as compared to NF. It provides strength to the proposed hypothesis and suggests more amorphous content for NR than NF.[73,86] The suppressed dispersive region indicates the high macroscopic dc conductivity and lies above the upper limit of current experimental range.

The frequency-dependent imaginary (σ'') part is shown in Figure 10(c,d). It may be noted from Figure 10(c,d) that in the high-frequency window the σ'' shows increase with frequency. Now, when we move from the high frequency to low frequency side then σ'' decreased and a peak is observed in the plot, that is, ω_{onset}.

At this frequency, the EP starts and σ'' increases continuously up to a peak frequency, that is, ω_{max}. The maxima associated corresponding to the peak ω_{max} indicates the full development of the EP. Furthermore, decrease of frequency shows the decrease in the σ'' and an identical trend is observed for all systems. All the polymeric systems show similar frequency dependence. The solid red line in the plot represents the simulated results (by Origin nonlinear curve fitting software) obtained by using the equations reported elsewhere.[58] It may be observed that both real and imaginary parts of the complex conductivity are in good agreement with the experimental results.

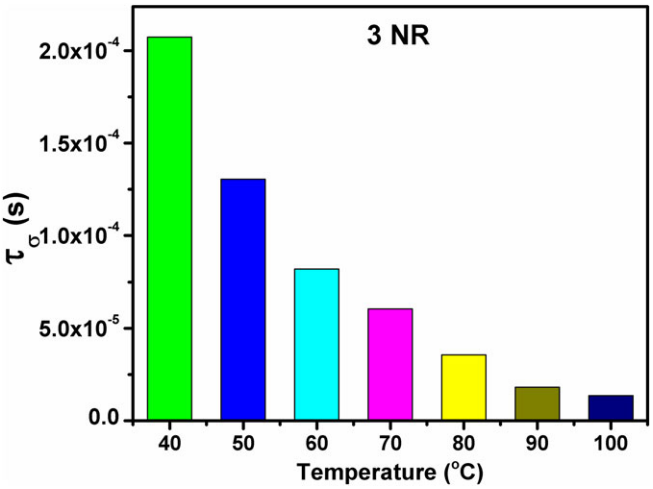

Figure 11. Variation of relaxation time (τ_σ) with temperature for 3NR system. [Color figure can be viewed at wileyonlinelibrary.com]

Figure 10(e,f) shows the temperature-dependent real and imaginary part of conductivity and the solid line shows the fitted plot. It may be noticed that with an increase of temperature EP region increases and dc conductivity region starts disappearing [-Figure 10(e)]. It confirms the thermally activated ion transportation and is the result of: (1) formation/breaking of coordinating sites and (2) increased the segmental motion of polymer chain. Figure 10(f) shows the shift of ω_{max} and ω_{on} toward high frequency and indicates the faster ion mobility in polymer matrix. The conductivity relaxation time was calculated using eq. (6):

$$\tau_\sigma = \frac{1}{2\pi f_{p(\sigma)}} \tag{6}$$

where $f_{p(\sigma)}$ is the frequency value corresponding to the σ'' spectra.[87] Figure 11 displays the variation of the relaxation time with temperature and decrease of relaxation time indicates the faster ion migration.

Modulus Formalism. The modulus spectroscopy is an important formalism as it suppresses the EP. Figure 12(a,b) displays the variation of real and imaginary parts of the modulus against the frequency at 40 °C. The low value in the low-frequency window is due to the minor contribution from the EP and increase with the increase of the frequency.[88] Figure 12 shows the low value of M' in the low frequency and indicate the ion migration via the conduction process.[89] In Figure 12(b), no transition peak was observed that may lie beyond the measured frequency range.

At the peak frequency, the transition from long-range to short-range ion mobility occurs when we move from low to high frequency and is termed as the frequency of conductivity relaxation. The flat region in the plot indicates the ion migration over long distances and is the result of large capacitance associated with

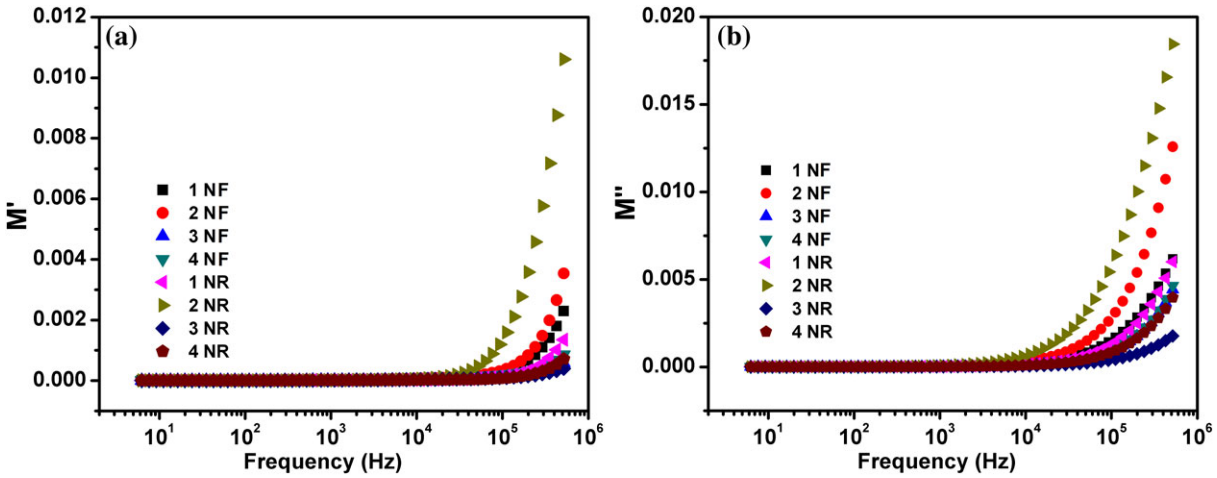

Figure 12. Frequency-dependent (a) real part and (b) imaginary part of complex modulus for polymer electrolyte dispersed with NF and NR. [Color figure can be viewed at wileyonlinelibrary.com]

EP.[90] The region which is not in the plot (above the experimental frequency range) evidences the ion confinement in the potential wells or short-range ion mobility. The low intensity of the M'' for the NR-based PNCs indicates the faster chain movement as compared to NF.[28,91] This confirms that the NR shaper nanoparticle is more effective in enhancing the ion migration.

Stability Analysis

Electrochemical Stability Window. Another key factor to check the feasibility of the SPE is electrochemical stability window (ESW). The voltage stability window was determined by sandwiching the PNC between symmetric SS electrodes (Configuration: SS|PNC|SS) over −3 to 3 V by LSV.[92] Figure 13 shows the LSV plot for the TiO_2 nanoparticle (NF and NR). For SPE with 1 NF voltage window has been found to be between ~4.2 (−2.2 to 2 V) and increases to 4.35 (−2.4 to 2 V) for the 4 NF system. While the right figure displays the voltage window with NR and obvious change occurs with a variation of nanoparticle content. Even at lower NR content (1NR) voltage window has been found larger (~4.35 V) than the NF system and increase up to ~4.8 V (i.e., −2.45 to 2.5 V). Although at about 5 V (i.e., at −2.5 and 2.5 V), an abrupt increase of current was observed which indicates the electrolyte decomposition.[93–95] It

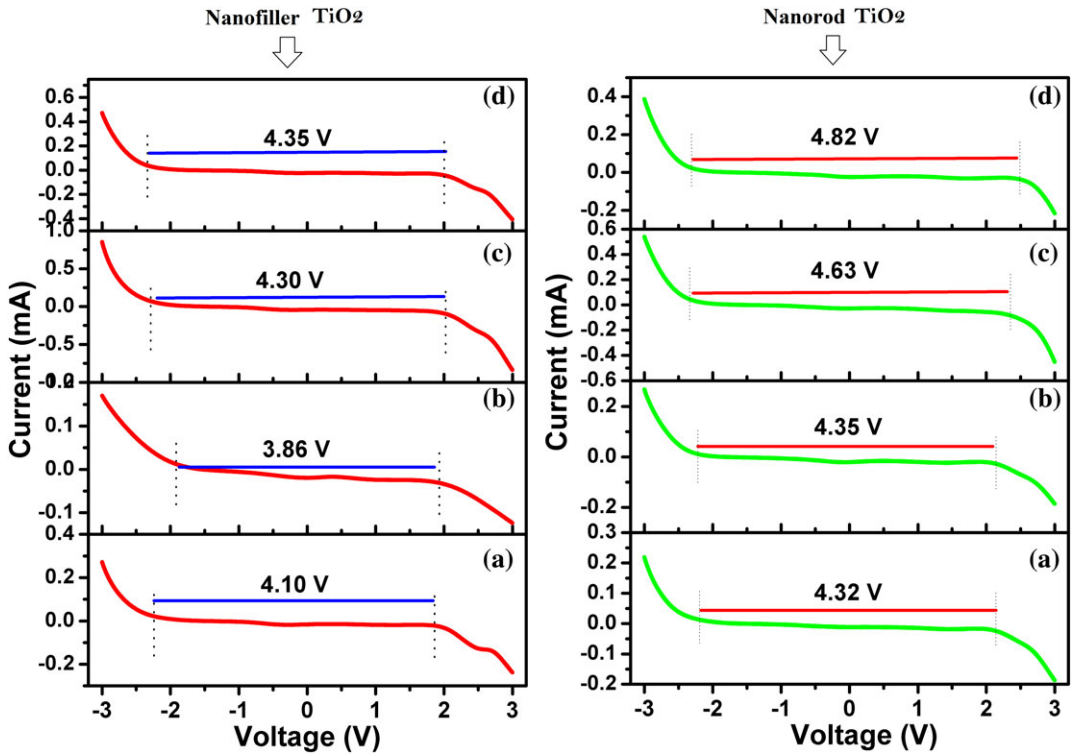

Figure 13. LSV of the SPE with TiO_2 NF and NR at room temperature. [Color figure can be viewed at wileyonlinelibrary.com]

Table II. Thermal Degradation and Char Content

Sample name	% Weight loss				Char content
	@ 100 °C	@ 200 °C	@ 300 °C	@ 400 °C	
Polymer salt	2.13	8.02	39.62	74.29	23.12
3NF	1.22	6.18	32.98	76.39	19.55
3NR	1.21	5.11	33.19	75.42	21.71

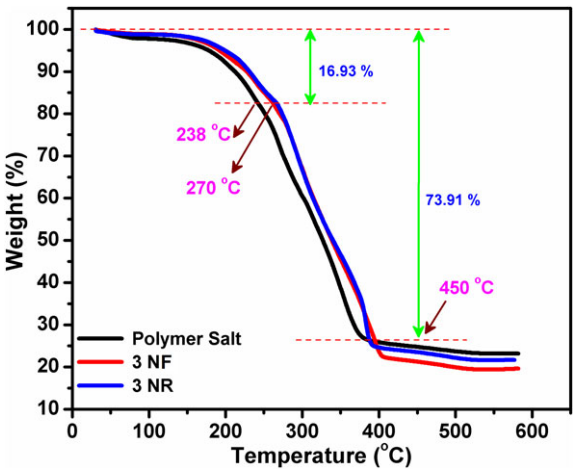

Figure 14. TGA curves of the PNCs films under N2 atmosphere at a heating rate of 10 °C. [Color figure can be viewed at wileyonlinelibrary.com]

may be noted that the SPE system with NR exhibits favorable and wider voltage stability window (~4–5 V) for real practical applications with safety in solid-state SIBs.

Thermogravimetric Analysis. The thermal stability is evaluated by TGA thermograms in terms of weight loss as a function of temperature for polymer salt and polymer salt dispersed with NF and NR under N_2 atmosphere at a scan rate of 10 °C. The slight weight loss below 100 °C may be due to the presence of moisture in the electrolyte and solvent evaporation. The negligible weight loss is observed for the polymer electrolyte dispersed with NF/NR (Figure 14). First decomposition temperature is at about 200 °C and shifts toward high temperature after the dispersion of NF/NR that indicates the enhanced thermal stability (Table II).

Furthermore, a weight loss of about 16.93 wt % is observed for the polymer salt complex @ 238°C and for the polymer salt dispersed with NF/NR is at @ 270°C. This shift of temperature directly evidences the increased thermal stability and NF/NR plays an effective role in slowing down the degradation mechanism.[96,97] The rapid decomposition in the temperature range 250–350 °C may be attributed to the decomposition of polymer and salt.[60] Even at high temperature (@ 400°C), the weight loss is not zero, still 26.09 wt % yield is there. It may be concluded from the TGA curves that the prepared PNC is thermally stable up to 250 °C.

CONCLUSIONS

In summary, we have studied the impact of shape of nanoparticle on the structural, electric, thermal, and dielectric properties of the SPE complexed with $NaPF_6$. All SPEs were prepared by the solution cast technique. From the FESEM analysis, it was found that surface morphology is altered with the addition of NF/NR and elemental mapping confirms the uniform dispersion in the polymer matrix. The complex formation was evidenced from the FTIR analysis and is influenced by the shape of the nanoparticle. The ionic conductivity is sensitive to the nanoparticle shape and we found that the NR dispersed system displays higher ionic conductivity than NF. This is attributed to the formation of long and continuous conduction paths for cation migration. The polymer electrolyte system with the highest ionic conductivity shows the lowest activation energy and follows the Arrhenius behavior. In addition, the ESW has been significantly improved with NR dispersion (~4.8 V) than NF dispersion (~4.2 V). The ionic transference number close to unity is obtained for nanoparticle-dispersed polymer electrolytes. The increase of the dielectric strength and ac conductivity was more for NR as compared to NF. The low value of relaxation time for NR-based system evidences the faster ion mobility and is in correlation with conductivity results. The complex conductivity and the complex permittivity are dependent on temperature and confirm the thermally activated process. The modulus formalism suggests the faster ion migration for NR-based system as compared to NF. The studies in the present work suggest that the ionic conductivity, ESW, ion transference number, and dielectric properties strongly depend on the shape of the nanoparticle, which may be adopted as a facile strategy to develop new polymer electrolytes for solid-state sodium ion batteries.

ACKNOWLEDGMENT

A.A. would like to acknowledge the financial assistance provided by the Central University of Punjab, Bathinda, India.

AUTHOR CONTRIBUTIONS

A.A. and A.L.S. designed and carried out the experimental work, data collection, interpretation of data, and drafted the manuscript. N.G.S. contributed to the preparation of NR and FESEM analysis of NR.

REFERENCES

1. Chen, R.; Qu, W.; Guo, X.; Li, L.; Wu, F. *Mater. Horiz.* **2016**, *3*, 487.
2. Song, F.; Li, W.; Sun, Y. *Inorganics*. **2017**, *5*, 40.
3. Li, W.; Wang, X.; Xiong, D.; Liu, L. *Int. J. Hydrogen Energy*. **2016**, *41*, 9344.
4. Li, W.; Gao, X.; Xiong, D.; Xia, F.; Liu, J.; Song, W. G.; Xu, J.; Thalluri, S. M.; Cerqueira, M. F.; Fu, X.; Liu, L. *Chem. Sci.* **2017**, *8*, 2952.
5. Zhang, J.; Zhang, C.; Li, W.; Guo, Q.; Gao, H.; You, Y.; Li, Y.; Cui, Z.; Jiang, K. C.; Long, H.; Zhang, D. *Xin. S. ACS Appl. Mater. Interfaces*. **2018**, *10*, 5543.
6. Li, X.; Wu, G.; Liu, X.; Li, W.; Li, M. *Nano Energy*. **2017**, *31*, 1.
7. Hou, G. M.; Zhang, M. Q.; Huang, Y. F.; Ruan, W. H. *RSC Adv.* **2016**, *6*, 83406.
8. Arya, A.; Sharma, A. L. *Ionics*. **2017**, *23*, 497.

9. Saykar, N. G.; Pilania, R. K.; Banerjee, I.; Mahapatra, S. *J. Phys. D: Appl. Phys.* **2018**, *51*, 475501.
10. Sharma, A. L.; Thakur, A. K. *Ionics*. **2013**, *19*, 795.
11. Perea, A.; Dontigny, M.; Zaghib, K. *J. Power Sources*. **2017**, *359*, 182.
12. Mindemark, J.; Lacey, M. J.; Bowden, T.; Brandell, D. *Prog. Polym. Sci.* **2018**, *81*, 114.
13. Hu, P.; Chai, J.; Duan, Y.; Liu, Z.; Cui, G.; Chen, L. *J. Mater. Chem. A*. **2016**, *4*, 10070.
14. Li, X.; Li, W.; Li, M.; Cui, P.; Chen, D.; Gengenbach, T.; Chu, L.; Liu, H.; Song, G. *J. Mater. Chem. A*. **2015**, *3*, 2762.
15. Sharma, A. L.; Shukla, N.; Thakur, A. K. *J. Polym. Sci. Part B: Polym. Phys.* **2008**, *46*, 2577.
16. Reddy Polu, A.; Kumar, R. *E-J. Chem.* **2011**, *8*, 347.
17. Berthier, C.; Gorecki, W.; Minier, M.; Armand, M. B.; Chabagno, J. M.; Rigaud, P. *Solid State Ion.* **1983**, *11*, 91.
18. Minier, M.; Berthier, C.; Gorecki, W. *J. Physique*. **1984**, *45*, 739.
19. Ratner, M. A.; Nitzan, A. *Faraday Discuss. Chem. Soc.* **1989**, *88*, 19.
20. Dürr, O.; Dieterich, W.; Nitzan, A. *Solid State Ion.* **2002**, *149*, 125.
21. Sharma, A. L.; Thakur, A. K. *Ionics*. **2009**, *16*, 339.
22. Moins, S.; Martins, J. C.; Krumpmann, A.; Lemaur, V.; Cornil, J.; Delbosc, N.; Decroly, N.; Dubois, P.; Lazzaroni, R.; Gohy, J. F.; Coulembier, O. *Chem. Commun.* **2017**, *53*, 6899.
23. Arya, A.; Sharma, A. L. *J. Phys. D: Appl. Phys.* **2017**, *50*, 443002.
24. Bhatt, C.; Swaroop, R.; Arya, A.; Sharma, A. L. *J. Mater. Sci. Eng. B*. **2015**, *5*, 418.
25. Arya, A.; Sadiq, M.; Sharma, A. L. *Ionics*. **2017**, *24*, 2295.
26. Elmahdy, M. M.; Chrissopoulou, K.; Afratis, A.; Floudas, G.; Anastasiadis, S. H. *Macromolecules*. **2006**, *39*, 5170.
27. Arya, A.; Sharma, A. L. *J. Phys. D: Appl. Phys.* **2018**, *51*, 045504.
28. Senthil Kumar, P.; Sakunthala, A.; Govindan, K.; Reddy, M. V.; Prabu, M. *RSC Adv.* **2016**, *6*, 91711.
29. Schaetzl, D. M.; Li, P.; Chaudhari, N.; Bernstein, G. H.; Fullerton-Shirey, S. K. *J. Phys. Chem. C*. **2014**, *118*, 18836.
30. Suo, L.; Borodin, O.; Wang, Y.; Rong, X.; Sun, W.; Fan, X.; Xu, S.; Schroeder, M. A.; Cresce, A. V.; Wang, F.; Yang, C.; Hu, Y. S.; Xu, K.; Wang, C. *Adv. Energy Mater.* **2017**, *7*, 1701189.
31. Dai, Z.; Mani, U.; Tan, H. T.; Yan, Q. *Small Methods*. **2017**, *1*, 1700098.
32. Jinisha, B.; Anilkumar, K. M.; Manoj, M.; Abhilash, A.; Pradeep, V. S.; Jayalekshmi, S. *Ionics*. **2018**, *24*, 1675.
33. Zhang, Z.; Xu, K.; Rong, X.; Hu, Y. S.; Li, H.; Huang, X.; Chen, L. *J. Power Sources*. **2017**, *372*, 270.
34. Gao, H.; Xin, S.; Xue, L.; Goodenough, J. B. *Chem*. **2018**, *4*, 833.
35. Mali, S. S.; Shim, C. S.; Park, H. K.; Heo, J.; Patil, P. S.; Hong, C. K. *Chem. Mater.* **2015**, *27*, 1541.
36. Arya, A.; Sharma, A. L. *J. Solid State Electrochem.* **2018**, *22*, 2725.
37. Choudhary, S.; Sengwa, R. J. *Polym. Bull.* **2015**, *72*, 2591.
38. Hashmi, S. A.; Upadhyaya, H. M.; Thakur, A. K.; Verma, A. L. *Ionics*. **2000**, *6*, 248.
39. Das, A.; Thakur, A. K.; Kumar, K. *Ionics*. **2013**, *19*, 1811.
40. Croce, F.; Appetecchi, G. B.; Persi, L.; Scrosati, B. *Nature*. **1998**, *394*, 456.
41. Anilkumar, K. M.; Jinisha, B.; Manoj, M.; Jayalekshmi, S. *Eur. Polym. J.* **2017**, *89*, 249.
42. Ni'Mah, Y. L.; Cheng, M. Y.; Cheng, J. H.; Rick, J.; Hwang, B. J. *J. Power Sources*. **2015**, *278*, 375.
43. Bao, J.; Qu, X.; Qi, G.; Huang, Q.; Wu, S.; Tao, C.; Gao, M.; Chen, C. *Solid State Ion.* **2018**, *320*, 55.
44. Tang, R.; Jiang, C.; Jian, J.; Liang, Y.; Zhang, X.; Wang, H.; Yang, H. *Appl. Phys. Lett.* **2015**, *106*, 022902.
45. Jonscher, A. K. Dielectric Relaxation in Solids; Chelsea Dielectric: London, **1983**.
46. Arya, A.; Sharma, A. L. *J. Int. Sci. Technol.* **2016**, *4*, 17.
47. Sharma, A. L.; Thakur, A. K. *J. Mater. Sci.* **2011**, *46*, 1916.
48. Xu, Q. F.; Liu, Y.; Lin, F. J.; Mondal, B.; Lyons, A. M. *ACS Appl. Mater. Interfaces*. **2013**, *5*, 8915.
49. Latif, F.; Aziz, M.; Katun, N.; Yahya, M. Z. *J. Power Sources*. **2006**, *159*, 1401.
50. Mohamad, A. A.; Mohamed, N. S.; Yahya, M. Z. A.; Othman, R.; Ramesh, S.; Alias, Y.; Arof, A. K. *Solid State Ion.* **2003**, *156*, 171.
51. Mohan, K. R.; Achari, V. B. S.; Rao, V. V. R. N.; Sharma, A. K. *Polym. Test.* **2011**, *30*, 881.
52. Howell, F. S.; Bose, R. A.; Macedo, P. B.; Moynihan, C. T. *J. Phys. Chem.* **1974**, *78*, 639.
53. Saminatha Kumaran, V.; Ng, H. M.; Ramesh, S.; Ramesh, K.; Vengadaesvaran, B.; Numan, A. *Ionics*. **2018**, *24*, 1947.
54. Cole, K. S.; Cole, R. H. *J. Chem. Phys.* **1941**, *9*, 341.
55. Cao, W.; Gerhardt, R. *Solid State Ion.* **1990**, *42*, 213.
56. Sharma, A. L.; Thakur, A. K. *Ionics*. **2015**, *21*, 1561.
57. Schonhals, A.; Kremer, F. Broadband Dielectric Spectroscopy; Springer: Berlin, Germany, **2003**. p. 59.
58. Roy, A.; Dutta, B.; Bhattacharya, S. *RSC Adv.* **2016**, *6*, 65434.
59. Sadiq, M.; Arya, A.; Sharma, A. L. Recent Trends in Materials and Devices. Vol. *178*; Springer International Publishing: Switzerland, **2017**. p. 389.
60. Patla, S. K.; Ray, R.; Asokan, K.; Karmakar, S. *J. Appl. Phys.* **2018**, *123*, 125102.
61. Arya, A.; Sharma, S.; Sharma, A. L.; Kumar, D.; Sadiq, M. *Asian J. Eng. Appl. Technol.* **2016**, *5*, 4.
62. Woo, H. J.; Majid, S. R.; Arof, A. K. *Mater. Chem. Phys.* **2012**, *134*, 755.
63. Tripathi, N.; Thakur, A. K.; Shukla, A.; Marx, D. T. *Polym. Eng. Sci.* **2018**, *58*, 220.

64. Ravi, M.; Pavani, Y.; Kiran Kumar, K.; Bhavani, S.; Sharma, A. K.; Narasimha Rao, V. V. R. *Mater. Chem. Phys.* **2011**, *130*, 442.
65. Karmakar, A.; Ghosh, A. *J. Appl. Phys.* **2010**, *107*, 104113.
66. Bergman, R.; Brodin, A.; Engberg, D.; Lu, Q.; Angell, C. A.; Torell, L. M. *Electrochim. Acta*. **1995**, *40*, 2049.
67. Karan, N. K.; Pradhan, D. K.; Thomas, R.; Natesan, B.; Katiyar, R. S. *Solid State Ion.* **2008**, *179*, 689.
68. Yusof, S. Z.; Woo, H. J.; Arof, A. K. *Ionics*. **2016**, *22*, 2113.
69. Truong, V. T.; Codd, A. R.; Forsyth, M. *J. Mater. Sci.* **1994**, *29*, 4331.
70. Arya, A.; Sharma, A. L. *J. Phys. Condens. Matter*. **2018**, *30*, 165402.
71. Woo, H. J.; Majid, S. R.; Arof, A. K. *Solid State Ion.* **2011**, *199–200*, 14.
72. Mohamed Ali, T.; Padmanathan, N.; Selladurai, S. *Ionics*. **2015**, *21*, 829.
73. Koduru, H. K.; Marino, L.; Scarpelli, F.; Petrov, A. G.; Marinov, Y. G.; Hadjichristov, G. B.; Iliev, M. T.; Scaramuzza, N. *Curr. Appl. Phys.* **2017**, *17*, 1518.
74. Kumar, M.; Srivastava, N. *Ionics*. **2015**, *21*, 1301.
75. Pal, P.; Ghosh, A. *Electrochim. Acta*. **2018**, *260*, 157.
76. Sharma, A. L.; Thakur, A. K. *Ionics*. **2010**, *17*, 135.
77. Scrosati, B.; Croce, F.; Persi, L. *J. Electrochem. Soc.* **2000**, *147*, 1718.
78. Choudhary, S.; Sengwa, R. J. *Mater. Chem. Phys.* **2013**, *142*, 172.
79. Kitajima, S.; Bertasi, F.; Vezzù, K.; Negro, E.; Tominaga, Y.; Di Noto, V. *Phys. Chem. Chem. Phys.* **2013**, *15*, 16626.
80. Money, B. K.; Hariharan, K.; Swenson, J. *J. Phys. Chem. B*. **2012**, *116*, 7762.
81. Das, S.; Ghosh, A. *Electrochim. Acta*. **2015**, *171*, 59.
82. Pal, P.; Ghosh, A. *Phys. Rev. E*. **2015**, *92*, 062603.
83. Funke, K. *Solid State Ion.* **1988**, *28–30*, 100.
84. Natesan, B.; Karan, N. K.; Katiyar, R. S. *Phys. Rev. E Stat. Nonlin. Soft Matter Phys.* **2006**, *74*, 042801.
85. Arya, A.; Sharma, A. L. *J. Mater. Sci.: Mater. Electron.* **2018**, *29*, 17903.
86. Telfah, A.; Abdul-Gader Jafar, M. M.; Jum'h, I.; Ahmad, M. J. A.; Lambert, J.; Hergenröder, R. *Polym. Adv. Technol.* **2018**, *29*, 1974.
87. Choudhary, S.; Sengwa, R. J. *Electrochim. Acta*. **2017**, *247*, 924.
88. Baral, A. K.; Narayanan, S.; Ramezanipour, F.; Thangadurai, V. *Phys. Chem. Chem. Phys.* **2014**, *16*, 11356.
89. Karmakar, A.; Ghosh, A. *Curr. Appl. Phys.* **2012**, *12*, 539.
90. Anada, Y. *Energy Procedia*. **2013**, *34*, 17.
91. Karmakar, A.; Ghosh, A. *Phys. Rev. E*. **2011**, *84*, 051202.
92. Sharma, A. L.; Thakur, A. K. *Appl. Polym. Sci.* **2010**, *118*, 2743.
93. Keller, M.; Appetecchi, G. B.; Kim, G. T.; Sharova, V.; Schneider, M.; Schuhmacher, J.; Roters, A.; Passerini, S. *J. Power Sources*. **2017**, *353*, 287.
94. Tao, C.; Gao, M. H.; Yin, B. H.; Li, B.; Huang, Y. P.; Xu, G.; Bao, J. J. *Electrochim. Acta*. **2017**, *257*, 31.
95. Prasanth, R.; Shubha, N.; Hng, H. H.; Srinivasan, M. *Eur. Polym. J.* **2013**, *49*, 307.
96. Joshi, M.; Raghavan, P.; Banerjee, K.; Thakare, V. *Indian J. Fiber Text. Res.* **2006**, *31*, 202.
97. Arya, A.; Sharma, A. L. *Appl. Sci. Lett.* **2016**, *2*, 72.